Journal Pre-proof

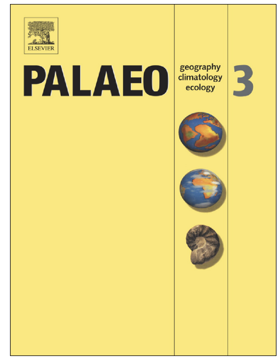

Diachronous end-Permian terrestrial ecosystem collapse with its origin in wildfires

Jing Lu, Ye Wang, Minfang Yang, Peixin Zhang, David P.G. Bond, Longyi Shao, Jason Hilton

PII: S0031-0182(22)00130-4

DOI: https://doi.org/10.1016/j.palaeo.2022.110960

Reference: PALAEO 110960

To appear in: *Palaeogeography, Palaeoclimatology, Palaeoecology*

Received date: 21 October 2021

Revised date: 21 March 2022

Accepted date: 24 March 2022

Please cite this article as: J. Lu, Y. Wang, M. Yang, et al., Diachronous end-Permian terrestrial ecosystem collapse with its origin in wildfires, *Palaeogeography, Palaeoclimatology, Palaeoecology* (2021), https://doi.org/10.1016/j.palaeo.2022.110960

Diachronous end-Permian terrestrial ecosystem collapse with its origin in wildfires

Jing Lu[a] lujing@cumtb.edu.cn, Ye Wang[a] bqt1900201012@student.cumtb.edu.cn, Minfang Yang[b] yangmf69@petrochina.com.cn, Peixin Zhang[a] pxzhang3963@163.com, David P. G. Bond[c,*] d.bond@hull.ac.uk, Longyi Shao[a] shaol@cumtb.edu.cn, Jason Hilton[d] j.m.hilton@bham.ac.uk

[a]State Key Laboratory of Coal Resources and Safe Mining, College of Geoscience and Surveying Engineering, China University of Mining and Technology, Beijing 100083, PR China

[b]Petroleum Exploration and Development Research Institute, PetroChina, Beijing100083, PR China

[c]Department of Geography, Geology and Environment, University of Hull, Hull, HU6 7RX, UK

[d]School of Geography, Earth and Environmental Sciences, University of Birmingham, Edgbaston, Birmingham B15 2TT, UK

[*]Corresponding author.

Editor Name: Dr. Paul Hesse

Abstract

The Permian-Triassic Mass Extinction (PTME) is the greatest biodiversity crisis in Earth history and while the marine crisis is increasingly well constrained, the timing and cause(s) of terrestrial losses remain poorly understood. There have been suggestions that the End-Permian Terrestrial Collapse (EPTC) pre-dated, was synchronous with or post-dated the marine crisis, or even occurred asynchronously in different regions. We address these conflicting interpretations through a detailed geochemical study of a terrestrial sequence in the Liujiang Coalfield on the North China Plate (NCP) in which we apply zircon U-Pb dating of tuffaceous claystone, kerogen identification, and analysis of organic carbon isotopic composition ($\delta^{13}C_{org}$), total organic carbon (TOC), continental weathering (via the chemical index of alteration; CIA) and Ni concentrations. Our study constrains the Permian-Triassic boundary (PTB) near the base of bed 20 in our sequence at approximately 251.9±1.1Ma, immediately above a Ni anomaly also known from other terrestrial sequences and the marine PTME. Organic carbon isotope chemostratigraphy together with evidence for algal blooms and the presence of mudstone clasts suggests that the onset of the EPTC in the NCP was synchronous with the crisis in low latitudes (e.g., South China), but was about 310 kyr later than the EPTC in higher southerly latitudes (e.g., Australia). The EPTC predates the marine PTME. Kerogen macerals suggest that a phase of increased wildfire was sustained from the onset of the EPTC in the NCP until the marine PTME interval, implicating wildfire as a major driver of the EPTC (at least in low latitudes) that, in turn, had devastating consequences for the marine realm.

Keywords: terrestrial ecosystem collapse, Permian-Triassic Mass Extinction, U-Pb dating, Ni concentration, organic carbon isotopes, North China Plate

1. Introduction

The Permian-Triassic Mass Extinction (PTME) is the largest mass extinction event in Earth history with as many as 90% of marine and 70% of terrestrial species wiped out (e.g., Erwin, 1994; Stanley, 2016). New biogeochemical modelling coupling the global Hg and C cycles indicates that a large, short-lived Hg spike and nadirs in the values of δ^{202}Hg and δ^{13}C at the beginning of the marine PTME interval are best explained by a sudden, massive pulse of terrestrial biomass oxidation caused by the collapse of terrestrial ecosystems (Dal Corso et. al., 2020). This lends support to the suggestion that terrestrial extinctions, collectively known as the End Permian Terrestrial Collapse (EPTC), towards the end of the Permian played a causal role in the marine crisis (e.g., Algeo et al., 2011).

Some earlier studies suggest that land plants suffered extinction significantly later than marine ecosystems (e.g., Looy et al., 2001), and later studies of the PTME suggest that terrestrial and marine ecosystems were devastated near-simultaneously at the end of the Permian (e.g., Shen et al., 2011). However, recent studies indicate that the terrestrial extinction (manifested as the disappearance of *Glossopteris*) occurred ~370 kyr earlier than the marine crisis in humid, high southerly latitudes such as the Sydney Basin in Australia (Fielding et al., 2019). In the Chinahe and Xiaohebian profiles in low-latitude humid regions of the northern hemisphere (South China), the terrestrial extinction (manifested as the disappearance of *Gigantopteris*) confirms the diachronous nature of extinctions, with those on land pre-dating the marine crisis (Biswas et al., 2020; Chu et al., 2020). Evaluation of the link between the two realms requires precise definition of timing of the EPTC and marine PTME across different climatic zones and ecological settings.

Emplacement of the Siberian Traps large igneous province - the leading candidate for the ultimate driver of the PTME - is characterized by three stages: pyroclastic eruptions, lava flow eruptions, and intrusions (Burgess et al., 2014, 2015). Previous studies have found that the onset of Siberian Traps intrusions are coincident with the maximum of the C-isotope negative excursion that is well known from the global P-T transition. This level marks the beginning of marine extinction losses, and this third stage of Siberian Traps volcanism is considered to be the main driver of the marine crisis (Burgess et al., 2014, 2015). However, the two earlier eruptive phases released relatively heavy carbon (with isotopic composition of ca. -6‰) that had a relatively minor effect on the global carbon cycle (Vervoort et al., 2019). The available evidence does not conclusively support a cause and effect relationship between the Siberian Traps and the terrestrial biological crisis because: 1) the purported causes of end-Permian terrestrial plant extinctions include wildfires (Chu et al., 2020), emissions of SO_2 and halogens that led to highly acidic rains (Maruoka et al., 2003), ozone depletion (Visscher et al., 2004; Benca et al., 2018) and increased UV-B radiation (Visscher et al., 2004; Foster and Afonin, 2005) are all controversial and it is not clear which, if any, of these are directly related to the Siberian Traps; and 2) recent research shows that island arc volcanism around the Tethys Ocean during the P-T transition might also have contributed to the end-Permian extinction (Zhang et al., 2021). To further complicate the northern vs. southern hemisphere extinction scenario, it has been shown that tropospheric and stratospheric circulation limited the flux of SO_4 from Siberian Traps to the southern hemisphere (Black et al., 2014). We perhaps should not expect the terrestrial extinctions in Australia and North China to be synchronous as they might have their origins in different drivers. This remains a fascinating aspect of the terrestrial crisis that requires further study.

We explore the relationship between the EPTC and marine PTME and the potential drivers of the former in a terrestrial sequence recorded in borehole cores from the Liujiang coalfield (NCP) by: 1) constraining the PTB using U-Pb dating of zircons; 2) correlating this terrestrial sequence with records of the marine PTME using $\delta^{13}C_{org}$ chemostratigraphy; 3) examining the record of soil erosion and algal blooms; and 4) assessing the relationship between wildfires and the terrestrial crisis through kerogen analysis.

2. Geological setting

During the Late Permian, the NCP was a cratonic inland depression basin located on the northeastern margin of the Paleo-Tethys Ocean (Fig. 1a) at approximately 20° N (Shang, 1997; Cao et al., 2019). The strata in our study area have their provenance in the Inner Mongolia uplift area of the northern NCP (Shang, 1997; Fig. 1b). Plant ranges are well known from this region (Wang and Zhang, 1997; Wang 2010; Fig. 1c) and reveal a stepwise and then abrupt loss of Cathaysian wetland species and ginkgophytes through the Wuchiapingian, followed by a major changeover at the end of the Wuchiapingian to a gymnosperm-dominated flora that is abruptly lost in the latest Changhsingian during the PTME (Wang and Zhang, 1997; Wang 2010). In this area, a continuous succession of Pennsylvanian to Permian strata reaches a thickness of about 500m, and includes (in ascending order) the Benxi, Taiyuan, Shanxi, Lower and Upper Shihhotse and Sunjiagou Formations (Shang, 1997). Our study focuses on the Sunjiagou Formation in the Liujiang coalfield at the northeastern margin of North China. The Sunjiagou Formation represents a succession of coal-free fluvial and lacustrine facies that were deposited in the Late Permian and varies from 80 to 200 m in thickness in North China (Shang, 1997). In the study area the Sunjiagou Formation is mainly composed of interbedded purplish red, gray-purple and gray-white feldspathic and quartzose sandstones, gravel-bearing quartz sandstones and purplish red mudstones (Shang, 1997). The top and bottom surfaces of the Sunjiagou Formation are likely diachronous across North China (Shang, 1997; Lu et al., 2021c). The study area became emergent in the Early Triassic (Induan) and younger Triassic strata are absent. The Indosinian movement at the end of the Middle Triassic resulted in the development of an angular, unconformable contact between the Permian to Induan strata and the overlying Xiahuayuan Formation, which is of Late Jurassic age (Shang, 1997). Our study focuses on the Changhsingian to earliest-Induan sequence.

3. Materials and analytical methods

Our study is based on two tuff samples and 28 mudstone samples taken from the ZK-3809 core that was drilled through the Sunjiagou Formation in the Liujiang coalfield. For radioisotopic dating of zircon grains, after crushing, grinding, sieving and heavy liquid and magnetic separation, euhedral zircon crystals that exhibited clear oscillatory zoning under the cathodoluminescence (CL) microscope were selected for U-Pb zircon isotope analysis. U-Pb dating was conducted at the State Key Laboratory of Geological Processes and Mineral Resources (Beijing) using a Thermo Fisher X-Series 2 ICP-MS instrument to acquire ion-signal intensities. Laser sampling was performed using a Coherent GeoLasPro-193nm system. Zircon 91500 and Plešovice zircon were used as external standards for U-Th-Pb isotopic ratios and for monitoring the standard of each analysis (Wiedenbeck et al., 1995, 2004; Sláma et al., 2008) respectively. Data Cal and Isoplot 3.0 software were used for age analysis, calculation, and the drawing of concordia diagrams from the ICP-MS data.

For other geochemical analyses, mudstone samples were crushed to a <1 mm powder and then divided into two parts. One part was prepared for kerogen enrichment and identification according to the China national standards (GB/T 19144-2010) and

(SY/T5125-2014) respectively, with no fewer than 300 effective points analyzed per sample. The remaining part of each mudstone sample was powdered to < 200 mesh and divided into four subparts for analysis of (1) organic carbon isotopes ($\delta^{13}C_{org}$); (2) total organic carbon (TOC); (3) major elements analysis; and (4) trace elements analysis. Each of these was performed at the Beijing Research Institute of Uranium Geology. $\delta^{13}C_{org}$ was measured by stable isotope mass spectrometry (Thermo Finnigan MAT253), and $\delta^{13}C_{org}$ values are expressed in per mille (‰) with respect to Vienna Pee Dee Belemnite (VPDB) with an absolute analysis error of ±0.1‰. Samples for TOC were first treated with phosphoric acid to remove inorganic carbon before TOC values were measured using a carbon-sulfur analyzer (Eltra CS580-A) with a lower detection limit of 100 ug/g (0.01%) in the low-carbon mode. The detection range in low-carbon mode is 10 ppm-5%, with an absolute analysis error of 20 ppm. Major element analysis was performed by X-ray fluorescence spectrometry (Philips PW2404) with a relative analysis error of ±5%. Trace element analysis was performed by inductively coupled plasma mass spectrometry (Thermo Finnigan MAT253) with a relative analysis error less than ±5%. Further details of analytical methods are described by Chu et al. (2020) and Lu et al. (2020).

4. Results and analysis

4.1. Lithology and stratigraphic sequence

The stratigraphic sequence through the Permian-Triassic interval (beds 1–22) is shown in Figure 2, and detailed sedimentary characteristics are shown in Figure 3. The lower part of the succession comprises red and green mudstones interbedded with sandstones. In the upper part, closer to the Permian-Triassic Boundary (PTB), beds 12 and 13 are horizontally bedded, gray and gray-green mudstones. Bed 14 is a gray-green siliceous rock mainly composed of amorphous opal and volcanic crystals containing small amounts of quartz and kaolinised feldspar (Fig. 3a, g, g1-g2). This is overlain by light gray mudstone and gray tuffaceous claystone (beds 15 and 16) respectively, while bed 17 is laminated gray-white sandstone (Fig. 3a, d-f). The gray sandstone of bed 18 is in angular contact with the underlying strata and contains a large number of subrounded to angular purple mudstone clasts (ranging in diameter from 0.5 cm to 5.5 cm). Bed 19 is a ca. 10 m thick, purplish-red mudstone containing subrounded purplish-red mudstone clasts (0.5 cm to 4 cm in diameter) and subrounded grayish-white clasts (0.5 cm to 1.5 cm in diameter; Fig. 3). Bed 20 is a ca. 9 m thick gray-green tuff composed of volcanic debris (~50%) and terrigenous clasts (~20%) within a tuffaceous matrix (~30%; Fig. 3a-b, b1-b4). The volcanic debris includes crystal fragments (mostly angular quartz plus minor feldspars and hornblendes) and detritus, plus small amounts of vitric fragments. The detritus is mainly rounded clasts (Fig. 3 b1-b4) suggestive of abrasion during transportation. The vitric fragments, which are mostly angular, are transparent under plane-polarized light and opaque under cross-polarized light. The terrigenous components are mainly rounded mudstone clasts while the tuffaceous matrix is mainly siliceous (Fig. 3c, d).

4.2. Zircon dating

Two tuffaceous claystones were sampled from Bed 20 from the uppermost part of the Sunjiagou Formation in the ZK3809 core. More than 3000 zircon crystals were separated from the stratigraphically lower sample (LJ 13) and 3500 zircon crystals were recovered from the higher sample (LJ 6). Zircons crystal sizes varied from 90–210 μm in diameter. Most crystals show euhedral morphology and clear oscillatory zoning in cathodoluminescence (CL; Fig. 4a). Th/U ratios for these zircon crystals vary from 0.33 to 1.56 (arithmetic mean ($\bar{x}$) = 0.65; Table 1). Collectively, these features indicate that these zircons are volcanic in origin (Yang et al., 2014; Lu et al., 2021a).

$^{206}Pb/^{238}U$ dating results for the two samples are shown in Figure 4 and Table 1. From sample LJ 13 at the bottom of the tuffite (Bed 20), 18 concordant age values yielded a weighted average of 251.9 ± 2.2 Ma (mean-squared weighted deviation [MSWD] = 0.038, n = 18, and uncertainties are given at the 2σ level), and a concordia age of 251.9 ± 1.1 Ma (MSWD=0.039). Thus, this tuffite layer began to form at ~251.9 Ma (Fig. 4c; Table 1). Two further analyzed zircons dated to 2511 to 2513 Ma (Table 1) record the basement age of the NCP (Qiao and Wang, 2014). From sample LJ 6 at the top of the tuffite horizon (bed 20), 18 zircons (varying from 249.0 to 252.5 Ma) yielded a weighted average of 251.6 ± 2.1 Ma (MSWD=0.024, n = 18, and uncertainties are given at the 2σ level), and a concordia age of 251.6 ± 1.1 Ma (MSWD=1.3), indicating that deposition of this tuffite layer ended at ~251.6 Ma (Fig. 4d; Table 1). Five further zircons from this level are dated to basement ages of 2505 to 2528 Ma (Table 1). The single-point analysis error of standard zircons Plešovice and 91500 is less than 1.8% (Table 1). Our zircon dating allows us to place the PTB close to the base of bed 20 at ~251.9 Ma.

4.3. $\delta^{13}C_{org}$, TOC and Ni Concentrations

Results of $\delta^{13}C_{org}$, TOC and Ni concentrations, Ni/Al ratios and kerogen macerals from the analysis of 28 mudstone samples are shown in Figure 2 and Table 2. $\delta^{13}C_{org}$ values vary from -28.6‰ to -23.1‰ with an average of -26.2‰, and our record includes two prominent negative excursions as well as a gradual positive excursion (Fig. 2a). The first negative excursion, of 2.2‰ (CIE I), occurs in the lower part of the Sunjiagou Formation (beds 3 to 5). This is followed by a gradual positive excursion in the middle part of the Sunjiagou Formation (beds 7 to 15). A second, larger negative excursion of 5.5‰ occurs near the top of the Sunjiagou Formation (beds 16 to 19, CIE II). Above this level, values remain stable between -27‰ and -28‰ (beds 19 to 20; Fig. 2a).

Total Organic Carbon values vary from 0.04% to 0.19% ($\bar{x}$ = 0.12%) and show a rising trend from 0.08% to 0.19% between beds 2 and 13 followed by a decreasing trend from 0.19% to 0.04% from beds 13 to 21 (Fig. 2b, Table 2).

Nickel concentrations range from 3.64 ppm to 34.78 ppm ($\bar{x}$ = 18.22 ppm) (Fig. 2c; Table 2). It has been suggested that Ni content is influenced by aluminum content (e.g. Fielding et al., 2019) and so we normalize Ni to Al and present our data in the form of Ni/Al ratios. These vary from 0.17×10^{-4} to 2.28×10^{-4} ($\bar{x} = 1.07\times10^{-4}$; Fig. 2e; Table 2). Both Ni and Ni/Al reveal a conspicuous peak at the base of bed 20.

4.4. Kerogen macerals and wildfire records

Inertinite content varies from 1.0% to 83.9% ($\bar{x}$ = 34.7%; Fig. 2g) of the total maceral content. Fusinite occurs in stable concentrations in the lower to middle parts of the Sunjiagou Formation, before an abrupt increase between beds 13 and 19 (from 1.0% to 83.9%).

Concentrations remain high in the upper part of Sunjiagou Formation (beds 18 and 19; Fig. 5e-h). Sapropelinite content varies between 1.5% and 90.0% ($\bar{x}$ = 20.8%) with the highest values found in bed 13. Exinite content varies between 0% and 27.8% ($\bar{x}$ = 6.6%) of which suberinite is the main component. The vitrinite group, with contents varying between 6.3% and 84.0% ($\bar{x}$ = 37.9%) is found in concentrations between 16.7% and 84.0% ($\bar{x}$ = 53.5%) between the lower and middle part of the Sunjiagou Formation before decreasing in the upper part (Fig. 5i–l).

The inertinite in the study area is entirely composed of fusinite (charcoal) which is opaque, pure black, and does not fluoresce under fluorescence illumination. The fusinite is mostly long and thin or fragmental in shape with sharp edges (Fig. 5a–d), indicating that it has not undergone significant transport. The provenance of the study area is the Inner Mongolia uplift to the north, which consists of eroded rocks of Precambrian age (Shang, 1997). Given that no plants existed on Earth at that time, it is impossible that fusinite could have been transported from the provenance lithologies to the study area. U/Th values vary from 0.21 to 0.37, and values <0.75 (Jones et al., 1994; Pattan et al., 2005) are considered to indicate that the same degree of oxidation is present through the vertical succession. Thus, we consider that the inertinite in the study area has not been reworked. Fusinite is considered to be the product of incomplete combustion (Guo and Bustin, 1998; Bustin and Guo, 1999), and it has been suggested that inertinite debris is common in the remains of peat following wildfires (e.g., Goodarzi, 1985, Glasspool and Scott, 2010; Scott, 2010). We consider that fusinite is a reliable proxy for wildfire in the study area during the time of deposition.

Journal Pre-proof

4.5. Weathering and the Chemical Index of Alteration

The degree of sedimentary recycling and potassium metasomatism alteration on the Chemical Index of Alteration (CIA) was evaluated using the Th/U ratio (c.f. Bhatia and Taylor, 1981) and the Al_2O_3-CaO* + Na_2O-K_2O (A-CN-K) diagram (Nesbitt and Young, 1984). The Th/U ratio varies from 2.65–4.79 (Table 2, Fig. 2h), indicating that the sedimentary source rocks in the study area are not recycled, since recycled mudrocks exhibit high Th/U ratios of around 6 due to oxidation of U^{4+} to U^{6+} and its removal as a soluble component (c.f. Bhatia and Taylor, 1981). This is in agreement with Shang (1997) who determined that sediments in the study area mainly derived from the Inner Mongolia Uplift. This is further demonstrated by the peak distribution of our zircon dating: the ages of the two samples (LJ 13 and LJ 6; bed 20) have bimodal distributions, with peaks of ~251Ma (36 zircons) and ~2500Ma (7 zircons) respectively. The older ages represent the age of the North China basement and those zircons derives from the Inner Mongolia Uplift to the north (Qiao and Wang, 2014). We are confident that the provenance of the study area is the Inner Mongolia Uplift to the north and that the sediments in the study area have not been affected by recycling. A reliability test of the CIA values in the study area was undertaken using an A-CN-K diagram (Nesbitt and Young, 1984) that shows the CIA values deviate from the ideal weathering trend line (Fig. 6) and are affected by potassium metasomatism. Subsequently, these CIA values were calibrated by the method of Fedo et al. (1995). The corrected values (CIA_{corr}) vary from 65.71–82.04 ($\bar{x}$=74.65) and show three periods of enhanced weathering in ascending order (Table 2, Fig. 2f), with the latter phases of enhanced weathering during the late Changhsingian corresponding to the EPTC and marine PTME respectively.

5. Discussion

5.1. The position of the PTB, terrestrial and marine extinction crises in the NCP

The PTB in the NCP is characterized, biostratigraphically, by a transition from the *Lueckisporites virkkiae* - *Jugasporites schaubergeroides* palynological assemblage of the Sunjiagou Formation to the *Aratrisporites – Lundbladispora – Triadispora* palynological assemblage of the Liujiagou Formation (Ouyang, 1982, 1999). In more recent studies, *Lundbladispora, Aratrisporites, and Taeniaesporites* and Triassic sporopollen markers were discovered in Liulin from Shanxi, placing the PTB 20m below the top of Sunjiagou Formation in North China (Hou and Ouyang, 2000). Although our borehole succession appears to be complete, it is impossible to reliably document plant fossil assemblages from such material (this requires field exposures). Therefore, we use our zircon U-Pb dating to constrain the PTB boundary for the first time in the NCP. Our zircon data yields a 251.9 ± 1.1 Ma age from the base of the tuff layer at the top of Sunjiagou Formation in the Liujiang Coalfield - an age very close to the age of the PTB in the International Chronostratigraphic Chart (251.902 ± 0.024Ma; Cohen et al., 2013, updated), but with larger error. Although the top of the Sunjiagou Formation has been eroded in the study area, the presence of the large, late Changhsingian CIE together with zircon dates (251.9Ma) for the base of bed 20 reliably constrain the PTB in the study area. The strata in this study are considered to provide a continuous record of the Changhsingian through the PTB in the Sunjiagou Formation.

In the well age-constrained Meishan section in South China the marine PTME began at

251.941 Ma, at which time the carbon isotope record shows a major negative excursion (~5.5‰). There is also an earlier, more modest negative carbon isotope excursion across the Wuchiapingian-Changhsingian boundary at Meishan, which aids correlation with our terrestrial record (Shen et al., 2011, 2013; Burgess et al., 2017; Fig. 7c). Previous studies have shown the Carboniferous and Permian lithostratigraphy of the NCP (including the Sunjiagou Formation) to be widely diachronous (Peng et al., 2003; Yang et al., 2020; Lu et al., 2021c). Most studies consider the Sunjiagou Formation to be of Changhsingian age (Wang et al., 2010; Yang, et al., 2012). A major marine Wuchiapingian-Changhsingian carbon isotope excursion has been noted by Shen et al. (2013). The CIE-I in our study is probably the same level, and thus we consider this to record the Wuchiapingian-Changhsingian boundary (from which level we calculated from the average sedimentary rate, Fig. 7c, d). However, we do not resolve the minor fluctuations recorded by Shen et al. (2013) within the overall negative excursion seen in the Liujiang coalfield.

A major late Changhsingian negative organic carbon isotope excursion is known from the terrestrial Chinahe and Xiaohebian profiles in South China (in the order of ~3.5‰ to ~5.5‰; Fig. 7e, f). The late Changhsingian marine and terrestrial carbon isotope excursions represent a global carbon cycle anomaly related to the PTME, and they provide a means to determine this level in our study area (Shen et al., 2011; Wu et al., 2020). We correlate the onset of the marine PTME to a level near the base of bed 19 in our succession, i.e. at the conclusion (low point) of CIE-II (Fig. 7d). This interpretation is supported by the presence of a Ni anomaly in the Liujiang coalfield succession at the base of bed 20 (our U-Pb defined PTB). A Ni anomaly is known from marine successions just below or at the level of the marine PTME and spanning the PTB (Kaiho et al., 2001; Burgess et al., 2015; Fielding et al., 2019). This widespread enhancement in sedimentary Ni concentrations around the level of the marine PTME suggests that Siberian Trap volcanism (the likely source of Ni) was a major driver of the end Permian die-off (Fig. 7b, d).

5.2. The EPTC in the NCP and global correlation

The position of end-Permian terrestrial plant extinctions in low-latitude South China and high-latitude Australia is manifest in the sedimentary record as the disappearance of *Gigantopteris* and *Glossopteris* respectively. However, plant preservation in the terrestrial red beds studied here is poor (and borehole samples are too small for systematic study of floras) and so we employ chemostratigraphy (e.g. Shen et al., 2011), the record of soil erosion (e.g., Kaiho et al., 2016; Xie et al., 2017), evidence for algal blooms (e.g. Fielding et al., 2019; Biswas et al., 2020; Mays et al., 2021), and chemical weathering (e.g. Algeo et al., 2010; Fielding et al., 2019) to constrain the EPTC interval in the study area. On the basis of each of these, we consider that:

(1) The EPTC initiated at the onset of the fall in $\delta^{13}C$ values associated with CIE-II (bed 12/13 contact), and persisted to the conclusion of this negative carbon isotope shift (in bed 19). Thus, the onset of this $\delta^{13}C$ excursion (CIE-II) is symptomatic of a collapse of terrestrial ecosystems (Shen et al., 2011; Biswas et al., 2020; Chu et al., 2020; Wu et al., 2020).

(2) Late Changhsingian soil erosion has been implicated as an indirect marker of terrestrial ecosystem collapse (Ward et al., 2000; Shen et al., 2011; Lu et al., 2020). A large amount of sub-angular to angular purplish-red mudstone debris appears in bed 18 of our

succession, which we interpret to be a result of increased soil erosion. This suggests that the terrestrial ecosystem collapse was well underway, or even concluded, by that level. As such, the EPTC in North China significantly predates both the global marine PTME and the PTB itself, in accordance with aforementioned plant fossil distributions (e.g., Wang and Wang, 1986; Wang, 1989; Cao et al., 2019). Soil erosion may have contributed to the proliferation of bacteria at the correlative level of the marine PTME in e.g., the Xiaohebian non-marine profile of South China (Biswas et al., 2020; Fig. 7b). Soil erosion is potentially both a cause, and consequence of, the extinction of life on land and subsequently in the oceans (Algeo et al., 2011, Kaiho et al., 2016, 2020; Wignall et al., 2020).

(3) The large quantities of sapropelinite found in bed 13 of our succession might have derived from algae living within the lake in which the studied sediments were deposited. Cyanobacterial blooms have also been identified in the non-marine profile of Xiaohebian in South China (Fielding et al., 2019; Biswas et al., 2020; Mays et al., 2021) where they are likely related to fertilization from products of the initial eruptive stages of the Siberian Traps large igneous province (LIP; Kaiho et al., 2020). Above our sapropelinite-rich bed, a layer of siliceous rocks (bed 14, SiO_2 content of 80%) possibly records the release of organic acids and CO_2 driven by the blooming and death of a large number of bacteria and algae (Fielding et al., 2019; Biswas et al., 2020). This could have created a locally acidic environment, conducive to the deposition of SiO_2-bearing sediment. As with the Xiaohebian succession, the algal bloom in our study occurred at the onset of the second negative carbon isotope excursion (CIE-II; Fig. 7d), further suggesting that Bed 13 marks the onset of the EPTC.

(4) The marine PTME occurred during a phase of enhanced continental weathering that

might have played a causal role in the crisis (Algeo and Twitchett, 2010). Enhanced weathering is also recorded in terrestrial sequences in the Sydney Basin of Australia, and at Yima and Shichuanhe in North China terrestrial extinction (Cao et al., 2019; Fielding et al., 2019). In our study area, two pulses of enhanced weathering during the late Changhsingian occurred at the levels at which we place the EPTC and the later stages of the marine PTME, including the PTB itself (Fig. 7d).

The EPTC in the study area can be correlated with the Dayulin profile in southern North China (Wu et al., 2020; Xing et al., 2021) using C-isotope chemostratigraphy and sporopollen data. At Dayulin, sporopollen and organic C-isotope chemostratigraphy reveal that the main plant species, including *Lycopsida* (*Densosporites*), *Filicopsida* (*Punctatisporites, Leiotriletes, Apiculatisportes*), *Pteridospermopsida* (*Cyclogranisporiea, Falcisporites, Alisparites*), *Conifers* (*Lueckisporites, Limitisporites, Klausipollenites, Lunatisporites, Floriniites*) and *Cycad/Ginkgoales* (*Cycadopites*) disappear (i.e. become extinct) about 12 m below the maximum negative peak in the carbon isotope record (Wu et al., 2020; Xing et al., 2021). In our study area, the level of the EPTC, inferred from multiple data, is 15 m below the peak in the negative C-isotope excursion. If we assume that the sedimentation rates were fairly consistent between the two sites, the EPTC occurred at Dayulin and in our study area near synchronously. Chemostratigraphic correlation with well-constrained palynological fossil evidence of the Dayulin profile supports our placement of the onset of EPTC in the study area.

Comparison of low-latitude North and South China records with those from higher, southerly latitudes such as the Sydney Basin of Australia suggests that the onset of the EPTC was diachronous. As shown, the onset of the terrestrial crisis was almost synchronous across North and South China, but this began ca. 310 kyr later than the collapse in Australia (Fig. 7c), based on high precision zircon dates from South China and Australia (Burgess et al., 2015; Fielding et al., 2019).

5.3. Wildfire and the end-Permian terrestrial crisis

The EPTC is manifest by the sudden and massive loss of plants and soils (Fielding et al., 2019; Chu et al., 2020). There is no consensus on the causal mechanism for this, with a plethora of posited drivers including volcanically-driven acid rain (Maruoka et al., 2003; Black et al., 2014), UV-B radiation-induced sterility due to ozone depletion (Visscher et al., 2004; Foster and Afonin, 2005; Benca et al., 2018), and seasonal climate change leading to an increase in wildfires (Chu et al., 2020), some or all of which might have contributed to a catastrophic loss of soils (Sephton et al., 2005) that has also been implicated in the marine PTME scenario (e.g. Algeo and Twitchett, 2010).

Of the various proposed terrestrial extinction drivers, wildfires are amongst the most frequently developed phenomena in the Late Permian of our study area. The concentration of inertinite in the study area increased dramatically towards the PTB (beds 13 to 20), with average concentrations of 68.1%, suggesting that wildfires became common at the northeast margin of the NCP at that time. Values of TOC show a decreasing trend following the EPTC, indicating that these wildfires caused the massive loss of land plant fuel. Similarly low TOC contents are known from terrestrial Yuzhou record (southern margin of North China; Lu et al., 2020) and in the marginal marine Shichuanhe section (Wu et al., 2020) suggesting a widespread trend. Despite the decrease in TOC content in the Lujiang coalfield, inertinite concentrations remain relatively high in the aftermath of the EPTC and this is likely because the plants of the NCP did not suffer total extinction - instead 11 genera with 16 species survived into the Triassic (Wang, 1989). Fire-derived products in terrestrial settings are found across the wider region in the run up to the marine PTME on the NCP (Baode and Yuzhou sections and this study), in South China (Guanbachong, Taoshujing, Lubei, Sandaogou, Dalongkou and Lengqinggou sections) and in Australia, suggesting that forest fire became common at that time (e.g., Shen et al., 2011; Yan et al., 2019; Chu et al., 2020; Lu et al., 2020; Vajda et al., 2020; Cai et al., 2021a, b; Figure 7).

The paleoclimate of the North China during the Late Permian varied from arid to semi-arid (Xing et al., 2021) and was therefore conducive to wildfires (Lu et al., 2020; Wu et al., 2020; Dal Corso et al., 2022). At the beginning of the EPTC, the increase in CIA values indicates that the climate was relatively wet, which likely suppressed wildfire activity. The occurrence of wildfires in the late Changhsingian might have been controlled by ignition mechanisms such as lightning (Lu et al., 2020). The data supports an increase in global runoff and a sharp increase in humidity around PTB (Algeo et al., 2010, 2011), but these increases in humidity might have been short-lived.

Increased wildfire activity would have resulted in large amounts of organic matter and nutrients produced by plant combustion and the associated enhanced weathering of soils and rocks to enter the oceans through surface runoff (Algeo et al., 2013). These large nutrient inputs provided the stimulus for blooms of cyanobacteria and algae (Biswas et al., 2020; Mays et al., 2021). We suggest that the wildfires responsible for the devastation of the land surface during the EPTC are causally linked to - via a cascade of effects - the subsequent marine PTME. The fire-promoting climatic effects of Siberian Traps, and potentially also island arc volcanism around the Tethys Ocean, initiated and were therefore a leading driver of the Permian-Triassic crisis on land and in the oceans.

6. Conclusions

We examined the relationship between terrestrial and marine losses during the Permian-Triassic Mass Extinction (PTME) in a terrestrial sequence from the North China Plate through a combined geochemical and petrographic study of borehole cores from the Liujiang coalfield. We conclude:

(1) Radiometric dating places the Permian-Triassic boundary (PTB) in the uppermost part of the Sunjiagou Formation on the North China Plate, where it is constrained by zircon dates to a tuffite layer at 251.9±1.1Ma.

(2) A large quantity of sapropelinite and purplish-red mudstone debris, interpreted to have resulted from catastrophic soil erosion, appear in the upper part of the Sunjiagou Formation prior to the level of the main (global and marine) PTME and the PTB. The onset of soil erosion marks the initiation of terrestrial ecosystem devastation (the End Permian Terrestrial Collapse, EPTC) in North China prior to the PTB.

(3) The onset of the collapse of terrestrial ecosystems in North China is marked by algal blooms and also corresponds to the initiation of a major negative carbon isotope excursion (CIE-II in bed 13). The EPTC concludes at the low point in this carbon isotope excursion

(bed 19). This globally widespread $\delta^{13}C_{org}$ excursion, of ~5.5‰, permits correlation of our record with the level of the marine PTME (that begins as the EPTC ends), and this confirms that ecological disturbance began in terrestrial settings in North China prior to the global marine crisis.

(4) The high fusinite content and low exinite and vitrinite contents suggests that frequent wildfires were responsible for the collapse of terrestrial ecosystems that led to soil erosion and the appearance of mudstone clasts in the sedimentary record in bed 18 of our succession. The timing of events as described above supports a temporal, and potentially causal relationship between wildfire, the EPTC, and the PTME in the oceans in which a cascade of catastrophic changes was induced by the fire-promoting climatic effects of Siberian Traps and Tethyan island arc volcanism.

Acknowledgments

We thank Suping Peng and Shifeng Dai (China University of Mining and Technology Beijing) for constructive discussions of the data, Jiahu Fang (China University of Mining and Technology Beijing) for assistance identifying kerogen macerals, and Jing He (Petroleum Exploration and Development, Changqing Exploration Bureau) for assistance with petrological analysis. We thank two anonymous reviewers for their constructive feedback on this manuscript. This work was supported by the National Natural Science Foundation of China (Grants 41772161, 4217021090), NERC (NE/P013724/1), the National Science and Technology Major Project (Award 2017ZX05009-002), and New Century Excellent Talents

Fund of Chinese Ministry of Education (Award no. 2013102050020). Funding enabled the authors to design the study, collect, analyse and interpret data, and to write the manuscript.

References

Algeo, T.J., Chen, Z.Q., Fraiser, M.L., Twitchett, R.J., 2011. Terrestrial-marine teleconnections in the collapse and rebuilding of Early Triassic marine ecosystems. Palaeogeog., Palaeoclimatol., Palaeoecol. 308, 1–11.

Algeo, T.J., Henderson, C.M., Tong, J.N., Feng, Q.L., Yin, H.F., Tyson, R.V., 2013. Plankton and productivity during the Permian-Triassic boundary crisis: an analysis of organic carbon fluxes. Glob. Planet. Change 105, 52–67. https://doi.org/10.1016/j. gloplacha.2012.02.008.

Algeo, T.J., Twitchett, R.J., 2010. Anomalous early Triassic sediment fluxes due to elevated weathering rates and their biological consequences. Geology 38, 1023–1026. https://doi.org/10.1130/G31203.1.

Benca, J.P., Duijnstee, I.A., Looy, C.V., 2018. UV-B–induced forest sterility: Implications of ozone shield failure in Earth's largest extinction. Sci. Advan. 4(2), p.e1700618.

Bhatia, M.R., Taylor, S.R., 1981. Trace-element geochemistry and sedimentary provinces: a study from the Tasman Geosyncline, Australia. Chem. Geol. 33, 115–125. https://doi.org/10.1016/0009-2541(81)90089-9.

Biswas, R.K., Kaiho, K., Saito, R., Tian, L., Shi, Z., 2020. Terrestrial ecosystem collapse and soil erosion before the end-Permian marine extinction: organic geochemical evidence from marine and non-marine records. Glob. Planet. Change 195, 103327.

Black, B.A., Lamarque, J.F., Shields, C.A., Elkins-Tanton, L.T., Kiehl, J.T., 2014. Acid rain and ozone depletion from pulsed Siberian Traps magmatism. Geology 42, 67–70.

Burgess, S.D., Bowring, S., Shen, S., 2014. High-precision timeline for Earth's most severe extinction. Proc. Natl. Acad. Sci. (USA) 111, 3316–3321.

Burgess, S.D., Bowring, S.A., 2015. High-precision geochronology confirms voluminous magmatism before, during, and after Earth's most severe extinction. Sci. Advan. 1, e1500470.

Burgess, S.D., Muirhead, J.D., Bowring, S.A., 2017. Initial pulse of Siberian Traps sills as the trigger of the end-Permian mass extinction. Nat. Comms 8, 164.

Bustin R. M., Guo Y., 1999. Abrupt changes (jumps) in reflectance values and chemical compositions of artificial charcoals and inertinite in coals. Int. J. Coal Geol. 38, 237–260.

Cai, Y. F., Zhang, H., Cao, C. Q., Zheng, Q. F., Jin, C. F., Shen, S. Z., 2021a, Wildfires and deforestation during the Permian-Triassic transition in the southern Junggar Basin, Northwest China. Earth-Sci. Rev. 218, 103670.

Cai, Y. F., Zhang, H., Feng, Z., Shen, S. Z., 2021b, Intensive wildfire associated with volcanism promoted the vegetation changeover in southwest China during the Permian−Triassic transition. Frontiers Earth Sci. 9, 615841.

Cao, C.Q., Wang, W., Jin, Y.G., 2002. Carbon isotope excursions across the Permian–Triassic boundary in the Meishan section, Zhejiang Province, China. Chin. Sci. Bull. 47, 1125–1129.

Cao, C.Q., Wang, W., Liu, L.J., Shen, S.Z., Summons, R.E., 2008. Two episodes of 13 C depletion in organic carbon in the latest Permian: evidence from the terrestrial sequences in northern Xinjiang, China. Earth Planet. Sci. Lett. 270, 251–257.

Cao, Y., Song, H.Y., Algeo, T.J., Chu, D.L., Du, Y., Tian, L., Wang, Y.H., Tong, J.N., 2019. Intensified chemical weathering during the Permian-Triassic transition recorded in terrestrial and marine successions. Palaeogeog., Palaeoclimatol., Palaeoecol., 519, 166–177.

Chu, D.L., Grasby, S.E., Song, H.J., Dal Corso, J., Wang, Y., Mather, T.A., Wu, Y.Y., Song, H.Y., Shu, W.C., Tong, J.N., Wignall, P.B., 2020. Ecological disturbance in tropical peatlands prior to marine Permian-Triassic mass extinction. Geology 48, 288–292.

Cohen, K.M., Finney, S.C., Gibbard, P.L., Fan, J.-X., 2013 (updated). The ICS International Chronostratigraphic Chart. Episodes 36, 199–204.

Dal Corso, J., Mills, B.J.W., Chu, D., Newton, R.J., Mather, T.A., Shu, W., Wu, Y., Tong, J., Wignall, P.B., 2020. Permo–Triassic boundary carbon and mercury cycling linked to terrestrial ecosystem collapse. Nat. Comms 11, 10.1038/s41467-020-16725-4.

Dal Corso, J., Song, H.J., Callegaro, S., Chu, D.L., Sun, Y.D., Hilton, J., Grasby, S.E., Joachimski, M.M., Wignall, P.B., 2022. Environmental crises at the Permian–Triassic mass extinction. Nat. Rev. Earth Environ. https://doi.org/10.1038/s43017-021-00259-4

Erwin D.H., 1994. The Permo-Triassic Extinction. Nature 376, 231–236.

Fedo, C.M., Nesbitt, H.W., Young, G.M., 1995. Unraveling the effects of potassium metasomatism in sedimentary-rocks and paleosols, with implications for paleoweathering conditions and provenance. Geology 23, 921–924. https://doi.org/10.1130/0091-7613(1995)023<0921

Fielding, C.R., Frank, T.D., McLoughlin, S., Vajda, V., Mays, C., Tevyaw, A.P., Winguth, A., Winguth, C., Nicoll, R.S., Bocking, M., Crowley, J.L., 2019. Age and pattern of the southern high-latitude continental end-Permian extinction constrained by multiproxy analysis. Nat. Comms. 10, 1-12.

Foster, C.B., Afonin, S.A., 2005. Abnormal pollen grains: an outcome of deteriorating atmospheric conditions around the Permian-Triassic boundary. J. Geol. Soc. Lond. 162, 653–659.

Glasspool, I.J., Scott, A.C., 2010. Phanerozoic concentrations of atmospheric oxygen reconstructed from sedimentary charcoal. Nat. Geoscience 3, 627–630.

Goodarzi F., 1985. Optically anisotropic fragments in a Western Canadian subbituminous coal. Fuel 64, 1294–1300.

Guo Y., Bustin R. M., 1998. FTIR spectroscopy and reflectance of modern charcoals and fungal decayed woods: implications for studies of inertinite in coals. International Journal of Coal Geology 37, 29—53.

Hou, J.P., Ouyang, S., 2000. Palynological flora of Sunjiagou Formation, Liulin, Shanxi. Acta Palaeontolog. Sin. 39, 356-368.

Jones. B., Manning. D. A. C., 1994. Comparison of geochemical indices used for the interpretation of palaeoredox conditions in ancient mudstones. Chem. Geol. 111, 111-129.

Kaiho, K., Aftabuzzaman, M.D., Jones, D.S., Tian, L., 2020. Pulsed volcanic combustion events coincident with the end-Permian terrestrial disturbance and the following global crisis. Geology 49, 289–293.

Kaiho, K., Kajiwara, Y., Nakano, T., Miura, Y., Kawahata, H., Tazaki, K., Ueshima, M., Chen, Z., and Shi, G.R. 2001. End-Permian catastrophe by a bolide impact; evidence of a gigantic release of sulfur from the mantle. Geology 29, 815–818.

Kaiho, K., Saito, R., Ito, K., Miyaji, T., Biswas, R., Tian, L., Sano, H., Shi, Z., Takahashi, S., Tong, J.N., Liang, L., Oba, M., Nara, F.W., Tsuchiya, N., Chen, Z.Q., 2016. Effects of soil erosion and anoxic-euxinic ocean in the Permian-Triassic marine crisis. Heliyon 2, e00137.

Looy, C.V., Twitchett, R.J., Dilcher, D.L., van Konijnenburg-Van Cittert, J.H., Visscher, H., 2001. Life in the end-Permian dead zone. Proc. Natl. Acad. Sci. (USA) 98, 7879–7883.

Lu, J., Zhang, P., Yang, M., Shao, L., Hilton, J., 2020. Continental records of organic carbon isotopic composition ($\delta^{13}C_{org}$), weathering, paleoclimate and wildfire linked to the End-Permian Mass Extinction. Chem. Geol. 558, 119764.

Lu, J., Wang, Y., Yang, M., Shao, L., and Hilton, J. 2021a. Records of volcanism and organic carbon isotopic composition (δ13Corg) linked to changes in atmospheric pCO2 and climate during the Pennsylvanian icehouse interval. Chem. Geol. 570, 120168. 10.1016/j.chemgeo.2021.120168

Lu, J., Zhang, P., Dal Corso, J., Yang, M., Wignall, P.B., Greene, S.E., Shao, L., Lyu, D., and Hilton, J. 2021b. Volcanically driven lacustrine ecosystem changes during the Carnian

Pluvial Episode (Late Triassic). Proceedings of the National Academy of Sciences 118:e2109895118. 10.1073/pnas.2109895118

Lu, J., Zhou, K., Yang, M., Zhang, P., Shao, L., Hilton, J. 2021c. Records of organic carbon isotopic composition (δ13Corg) and volcanism linked to changes in atmospheric *p*CO2 and climate during the Late Paleozoic Icehouse. Glob. Planet. Change 207, 103654. 10.1016/j.gloplacha.2021.103654

Maruoka, T., Koeberl, C., Hancox, P.J., Reimold, W.U., 2003. Sulfur geochemistry across a terrestrial Permian-Triassic boundary section in the Karoo Basin, South Africa. Earth Planet. Sci. Lett. 206, 101–117.

Mays, C., McLoughlin, S., Frank, T.D., Fielding, C.R., Slater, S.M., Vajda, V. 2021. Lethal microbial blooms delayed freshwater ecosystem recovery following the end-Permian extinction. Nature Communications 12, 5511.

Nesbitt, H.W., Young, G.M., 1984. Prediction of some weathering trends of plutonic and volcanic rocks based on thermodynamic and kinetic considerations. Geochim. Cosmochim. Acta 48, 1523–1534. https://doi.org/10.1016/0016-7037(84)90408-3.

Ouyang, S., Hou, J.P., 1979. Characteristics of the Cathaysian palynological flora. Acta Palaeontolog. Sin. 3, 23–28.

Ouyang, S., Zhang, Z.L., 1982. Early Triassic palynological assemblages from Dengfeng, Henan. Acta Palaeontolog. Sin. 6, 21.

Pattan, J.N., Pearce, N.J.G., Mislankar, P.G. 2005. Constraints in using Cerium-anomaly of bulk sediments as an indicator of paleo bottom water redox environment: A case study from the Central Indian Ocean Basin. Chem. Geol. 221, 260–278. 10.1016/j.chemgeo.2005.06.009

Peng, Y., Chen, Y., Liu, Y., 2003. Benxi Formation – lithohorizon and chronohorizon with diachronism. Glob. Geol. 22, 111–118.

Qiao, X.F., Wang, Y.B., 2014. Lower Mesoproterozoic age and basin characteristics of the North China Craton. Acta Geol. Sin. 9, 1621–1637

Scott, A.C., 2010. Charcoal recognition, taphonomy and uses in palaeoenvironmental analysis. Palaeogeog., Palaeoclimatol., Palaeoecol. 291, 11–39.

Sephton, M.A., Looy, C.V., Brinkhuis, H., Wignall, P.B., De Leeuw, J.W., Visscher, H., 2005. Catastrophic soil erosion during the end-Permian biotic crisis. Geology 33, 941–944.

Shang, G.X., 1997. The Late Paleozoic coal geology of North China Platform, Taiyuan. Shanxi Science and Technology Press, Taiyuan, pp. 1–160.

Shen W.J., Lin Y.T., Sun Y.G., G., Xu L., Zhang H., 2008. Black carbon record in Permian-Triassic transitional strata of Meishan section, Changxing County, Zhejiang Province and its geological significance. Acta Petrolog. Sin., 24 (10): 2407–2414

Shen, S.Z., Cao, C.Q., Zhang, H., Bowring, S.A., Henderson, C.M., Payne, J.L., Davydov., V.I., Chen, B., Yuan, D.X., Zhang, Y.C., Wang, W., Zheng, Q.F., 2013. High-resolution $\delta^{13}C_{carb}$ chemostratigraphy from latest Guadalupian through earliest Triassic in South China and Iran. Earth Planet. Sci. Lett. 375, 156–165.

Shen, S.Z., Crowley, J. L., Wang, Y., Bowring, S.A., Erwin, D.H., Sadler, P.M., Cao, C.Q., Rothman, D.H., Henderson, C.M., Ramezani, J., Zhang, H., Shen, Y.A., Wang, X.D., Wang, W., Mu, L., Li, W.Z., Tang, Y.G., Liu, X.L., Liu, L.J., Zheng, Y., Jiang, Y.F., Jin, Y.G. 2011. Calibrating the End-Permian Mass Extinction. Science 334, 1367–1372.

Sláma, J., Košler, J., Condon, D.J., Crowley, J.L., Gerdes, A., Hanchar, J.M., Horstwood, M.S.A., Morris, G.A., Nasdala, L., Norberg, N., Schltegger, U., Schoene, B., Tubrett, M.N., Whitehouse, M.J. 2008. Plešovice zircon - A new natural reference material for U–Pb and Hf isotopic microanalysis. Chem. Geol. 249, 1–35.

Stanley, S.M., 2016. Estimates of the magnitudes of major marine mass extinctions in earth history. Proc. Natl. Acad. Sci. (USA) 113, E6325-E6334.

Vajda, V., McLoughlin, S., Mays, C., Frank, T.D., Fielding, C.R., Tevyaw, A., Lehsten, V., Bocking, M., and Nicoll, R.S. 2020. End-Permian (252 Mya) deforestation, wildfires and flooding—An ancient biotic crisis with lessons for the present. Earth Planet. Sci. Lett. 529, 115875. 10.1016/j.epsl.2019.115875

Visscher, H., Looy, C.V., Collinson, M.E., Brinkhuis, H., Van Konijnenburg-Van Cittert, J.H., Kürschner, W.M., Sephton, M.A., 2004. Environmental mutagenesis during the end-Permian ecological crisis. Proc. Natl. Acad. Sci. (USA) 101, 12952–12956.

Vervoort, P., Adloff, M., Greene, S.E., Kirtland Turner, S., 2019. Negative carbon isotope excursions: an interpretive framework. Environ. Res. Lett. 14, 85014. https://doi. org/10.1088/1748-9326/ab3318.

Wang Z.Q., 1989. The Permian macrophyte event in North China. Acta Palaeontolog. Sin. 28, 314–343.

Wang Z.Q., Wang L.X., 1986. Late Permian plant fossils in the lower part of Shiqianfeng Group, North China. Tianjin Institute of Geology and Mineral Resources, Chinese Academy of Geological Sciences 15, 1–13.

Wang, J., 2010. Late Paleozoic macrofloral assemblages from Weibei Coalfield, with reference to vegetational change through the Late Paleozoic Ice-age in the North China Block. Int. J. Coal Geol. 83, 292–317.

Wang, Z.Q., Zhang, Z.P., 1997. Gymnosperms and their survival strategies before the extinction of the late Permian colonies in North China. Chinese Sci. Bull. 20, 8–15.

Ward, P.D., Montgomery, D.R., Smith, R., 2000. Altered river morphology in South Africa related to the Permian–Triassic extinction. Science 289, 1740–1743.

Wiedenbeck, M., Alle, P., Corfu, F., Griffin, W.L., Meier, M., Oberli, F., Vonquadt, A., Roddick, J.C., Spiegel, W., 1995. Three natural zircon Standards for U-Th-Pb, Lu-Hf, trace-element and REE analyses. Geostandards Newsletter 19, 1–23.

Wiedenbeck, M., Hanchar, J.M., Peck, W.H., Sylvester, P., Valley, J., Whitehouse, M., Kronz, A., Morishita, Y., Nasdala, L., Fiebig, J., Franchi, I., Girard, J.-P., Greenwood, R.C., Hinton, R., Kita, N., Mason, P.R.D., Norman, M., Ogasawara, M., Piccoli, P.M., Rhede, D., Satoh, H., Schulz-Dobrick, B., Skår, O., Spicuzza, M.J. Terada, K., Tindle, A., Togashi, S., Vennemann, T., Xie, Q. Zheng, Y.-F., 2004. Further characterisation of the 91500 zircon crystal. Geostand. Geoanalytical Res. 28, 9–39.

Wignall, P.B., Chu, D.L., Hilton, J.M., Dal Corso, J., Wu, Y., Wang, Y., Atkinson, J., Tong, J.N., 2020. Death in the shallows: The record of Permo-Triassic mass extinction in paralic settings, southwest China. Glob. Planet. Change 198, 103176.

Wu, Y.Y., Tong, J.N., Algeo, T.J., Chu, D.L., Cui, Y., Song, H.Y., Shu, W.C., Du, Y., 2020, Organic carbon isotopes in terrestrial Permian-Triassic boundary sections of North China: Implications for global carbon cycle perturbations: GSA Bulletin 132, 1106–1118.

Xie, S., Algeo, T.J., Zhou, W., Ruan, X., Luo, G., Huang, J., Yan, J., 2017. Contrasting microbial community changes during mass extinctions at the Middle/Late Permian and Permian/Triassic boundaries. Earth Planet. Sci. Lett. 460, 180–191.

Xie, S., Pancost, R.D., Huang, J., Wignall, P.B., Yu, J., Tang, X., Chen, L., Huang, X., Lai, X., 2007. Changes in the global carbon cycle occurred as two episodes during the Permian–Triassic crisis. Geology 35, 1083–1086.

Xie, S., Pancost, R.D., Yin, H., Wang, H., Evershed, R.P., 2005. Two episodes of microbial change coupled with Permo/Triassic faunal mass extinction. Nature 434, 494–497.

Xing, Z. F., Fu, Y.X., Zheng, W., Li D., Li, S.P., Liu, Y.L., Qi, Y.A., Li, W.Y., Xu, X., Wu, P.P., Zhang X. Y., 2021. Sporopollen assemblage of upper Permian Sunjiagou Formation in Yiyang, western Henan and its geological significance. J. Palaeogeography 23, 901–918.

Yan, M. X., Wan, M. L., He, X. Z., Hou, X. D., Wang, J. 2016. First report of Cisuralian (early Permian) charcoal layers within a coal bed from Baode, North China with reference to global wildfire distribution. Palaeogeogr. Palaeoclimatol. Palaeoecol. 459, 394–408. doi:10.1016/j.palaeo.2016.07.031

Yan, Z.M., Shao, L., Glasspool, I.J., Wang, J., Wang, X.T., Wang, H., 2019. Frequent and intense fires in the final coals of the Palaeozoic indicate elevated atmospheric oxygen levels at the onset of the end-Permian mass extinction event. Int. J. Coal Geol. 207, 75–83.

Yang, G.X., Wang, H.S., 2012. Yuzhou Flora-a hidden gem of the Middle and Late Cathaysian Flora. Sci. China Earth Sci. 55, 1601–1619. https://doi.org/10.1007/s11430-012-4476-2.

Yang, J., Cawood, P.A., Monta˜nez, I.P., Condon, D.J., Du, Y., Yan, J., Yan, S., Yuan, D., 2020. Enhanced continental weathering and large igneous province induced climate warming at the Permo-Carboniferous transition. Earth Planet. Sci. Lett. 534, 116074.

Zhang, H., Zhang, F., Chen, J.B., Erwin, D.H., Syverson, D.D., Ni, P., Rampino, M., Chi, Z., Cai, Y.F., Xiang, L., Li, W.Q., Liu, S.A., Wang, R.C., Wang, X.D., Feng, Z., Li, H.M., Zhang, T., Cai, H.M., Zheng, W., Cui, Y., Zhu, X.K., Hou, Z.Q., Wu, F.Y., Xu, Y.G., Planavsky, N., Shen, S.Z. 2021. Felsic volcanism as a factor driving the end-Permian mass extinction. Science Advances 7:h1390. 10.1126/sciadv.abh1390

Figure 1. Location and geological context for the study area including a) Lopingian paleogeography showing position of the North China Plate (NCP; modified from Shen et al., 2013); b) Paleogeographic map of the NCP during deposition of the Sunjiagou Formation showing the position of the Liujiang Basin (modified from Shang, 1997; black arrow represents the direction of source); and c) Stratigraphic distributions of plant megafossil and palynological taxa and biozones (modified from Wang and Zhang, 1997; Wang, 2010).

Figure 2. The full stratigraphic sequence showing key events and a) $\delta^{13}C_{org}$; b) total organic

carbon; c) Ni concentrations; d) Ni/Al ratios; e) CIA values, f) kerogen macerals, and g) Th/U ratios in the ZK3809 core. Abbreviations: Permian-Triassic Mass Extinction (PTME); EPTC = End Permian Terrestrial Collapse.

Figure 3. Lithology, stratigraphic sequence and mass extinction events during the Permian-Triassic transition: a) log showing beds 12-20 in the Sunjiaguo Formation including the position of the mudstone clasts and the samples imaged in panels b-i; b1-b4) quartz, feldspar crystal fragments and rigid detritus from bed 20; g1-g2) photomicrographs of sections of vitric pyroclasts of volcanic origin from bed 14. Abbreviations: F. = Formation; B. = Bed; Litho. = Lithology; Qc- Quartz crystal fragment; Rd- Rigid debris; F- Feldspar crystal fragment.

Figure 4. Zircon U-Pb concordia diagrams of samples LJ 13 and LJ 6: a) zircon crystals from each sample; b) age of sample LJ 13; c) age of sample LJ 6.

Figure 5. Photomicrographs showing microstructural characteristics of kerogen macerals in the study area: a) overview showing characteristics of fusinite (transmitted light, sample LJ 19); b-d) fusinite (transmitted light, samples LJ 18 and LJ 19); e-f) sapropelinite (transmitted light and fluorescence, respectively, sample LJ 32); g-h) enlarged sapropelinite (transmitted light and fluorescence, respectively, sample LJ 32); i-j) vitrinite (transmitted light, samples LJ 16, and LJ 39); k-l) suberinite (transmitted light, samples LJ 11 and LJ 17).

Figure 6. A-CN-K diagram of mudstone samples from Changhsingian to early Induan with the chemical index of alteration (CIA) scale to the left, showing the possible influence of potassium metasomatism. For comparison, the average upper crust CIA value of southern part and the interior of the North China Craton are shown (modified from Cao et al., 2019). Abbreviations: A = Al_2O_3; CN = CaO* + Na_2O; K = K_2O; CIA = chemical index of alteration; Ka = kaolinite; Gi = gibbsite; Il = illite; PI = Plagioclase; Chl = chlorite; Sm = smectite; Ksp = K-feldspar; INCC = Interior North China Craton; SNCC = Southern North China Craton.

Figure 7. Summary and correlation of carbon isotope records, Ni and Ni/Al concentrations between marine PTB sequences at its global stratotype at c) Meishan, China; and a, d-f) terrestrial sequences studied here and known from the literature (Sydney Basin from Fielding et al., 2019 and Vajda et al., 2020, the ZK3809 core from North China in this study, Xiaohebian in South China from Biswas et al., 2020, and the Chinahe in South China from Chu et al., 2020). The $\delta^{13}C_{carb}$ data for Meishan are from Cao et al. (2002), Shen et al. (2011) and Burgess et al. (2014). High precision dating of Meishan comes from Burgess et al. (2015). Enhanced weathering and soil erosion data for Meishan is from Algeo et al. (2011). Enhanced wildfire data for Meishan is from Shen et al. (2008). Ni concentrations for Meishan are from Kaiho et al., 2001. The Siberian Traps LIP timeline (b) is from Burgess et al. (2017).

Table 1. Zircon U-Pb dating isotope results for tuffite samples LJ 6 and LJ13.

Sample number	Zircon sample number	Content(μg/g)		Th/U	Isotope ratios				rho	Age		Concordance
		Th	U		$^{207}Pb/^{235}U$	$^{207}Pb/^{235}U$	$^{206}Pb/^{238}U$	$^{206}Pb/^{238}U$		$^{206}Pb/^{238}U$	$^{206}Pb/^{238}U$	
		232	238		Ratio	1sigma	Ratio	1sigma		Age (Ma)	1sigma	

	LJ6-2	233.8	457.1	0.51	0.3062	0.0210	0.0399	0.0006	0.2158	252.2	3.7	92%
	LJ6-3	99.3	171.3	0.58	0.2804	0.0250	0.0398	0.0011	0.3157	251.7	7.0	99%
	LJ6-6	139.3	287.2	0.49	0.2853	0.0188	0.0400	0.0007	0.2833	252.5	4.6	99%
	LJ6-7	724.9	898.4	0.81	0.2845	0.0350	0.0394	0.0010	0.2053	249.0	6.2	97%
	LJ6-8	117.5	156.4	0.75	0.2671	0.0208	0.0398	0.0009	0.2830	251.9	5.4	95%
	LJ6-12	202.4	228.8	0.88	0.2662	0.0216	0.0399	0.0008	0.2430	252.3	4.9	94%
	LJ6-13	366.5	860.1	0.43	0.2641	0.0142	0.0398	0.0007	0.2399	251.7	4.5	94%
	LJ6-14	162.8	222.0	0.73	0.2783	0.0174	0.0397	0.0007	0.3002	251.1	4.6	99%
	LJ6-15	227.3	275.0	0.83	0.2826	0.0387	0.0397	0.0009	0.1616	250.9	5.4	99%
	LJ6-16	95.5	196.5	0.49	0.2784	0.0156	0.0397	0.0008	0.3421	250.7	4.7	99%
LJ6	LJ6-17	464.0	834.1	0.56	0.2807	0.0143	0.0397	0.0006	0.2811	251.1	3.5	99%
	LJ6-18	747.7	861.5	0.87	0.2784	0.0109	0.0398	0.0006	0.4009	251.8	3.9	97%
	LJ6-20	209.0	614.6	0.34	0.2797	0.0124	0.0399	0.0006	0.3506	252.1	3.8	99%
	LJ6-21	113.7	154.4	0.74	0.2791	0.0221	0.0399	0.0009	0.2808	252.4	5.5	99%
	LJ6-22	380.1	471.1	0.81	0.2766	0.0177	0.0399	0.0008	0.2944	252.2	4.7	98%
	LJ6-23	152.9	292.8	0.52	0.2751	0.0154	0.0398	0.0007	0.3076	251.4	4.2	98%
	LJ6-24	165.8	333.4	0.50	0.2840	0.0174	0.0398	0.0008	0.3098	251.3	4.7	99%
	LJ6-25	266.0	360.3	0.74	0.2671	0.0172	0.0399	0.0007	0.2846	252.0	4.5	95%
	LJ6-4	185.4	317.4	0.58	11.0269	0.3257	0.4846	0.0064	0.4470	2547.1	27.8	99%
	LJ6-9	292.0	344.6	0.85	9.9281	0.8537	0.4726	0.0248	0.6113	2494.9	108.8	97%
	LJ6-19	36.0	75.2	0.48	11.4538	0.3663	0.4804	0.0078	0.5050	2528.9	33.8	98%
	LJ6-27	532.9	340.8	1.56	10.2572	0.9921	0.4750	0.0390	0.8493	2505.3	170.5	98%

	LJ6-28	327.0	267.5	1.22	10.4758	0.3157	0.4790	0.0068	0.4724	2522.7	29.7	98%
LJ13	LJ13-2	147.8	286.5	0.52	0.2795	0.0156	0.0398	0.0006	0.2909	251.9	4.0	99%
	LJ13-4	252.4	502.5	0.50	0.2937	0.0132	0.0399	0.0006	0.3570	252.1	4.0	96%
	LJ13-5	70.9	107.6	0.66	0.2760	0.0320	0.0399	0.0010	0.2251	252.3	6.5	98%
	LJ13-6	72.8	163.0	0.45	0.2811	0.0319	0.0400	0.0016	0.3433	252.9	9.7	99%
	LJ13-8	38.0	94.8	0.40	0.2835	0.0270	0.0397	0.0013	0.3315	250.9	7.8	98%
	LJ13-9	70.8	106.1	0.67	0.2870	0.0269	0.0397	0.0010	0.2567	251.0	5.9	97%
	LJ13-11	56.6	82.5	0.69	0.2849	0.0264	0.0396	0.0011	0.3088	250.2	7.0	98%
	LJ13-12	94.1	201.1	0.47	0.2737	0.0215	0.0400	0.0008	0.2706	252.6	5.3	97%
LJ13	LJ13-14	535.4	915.6	0.58	0.2751	0.0125	0.0399	0.0005	0.2999	252.4	3.4	97%
	LJ13-15	372.5	642.2	0.58	0.2769	0.0127	0.0395	0.0006	0.3294	250.0	3.7	99%
	LJ13-16	473.1	675.4	0.70	0.2791	0.0166	0.0399	0.0006	0.2718	252.1	4.0	99%
	LJ13-18	162.4	333.2	0.49	0.2850	0.0163	0.0399	0.0007	0.2882	252.4	4.1	99%
	LJ13-19	247.7	433.0	0.57	0.2853	0.0267	0.0401	0.0008	0.2099	253.2	4.9	99%
	LJ13-21	70.9	121.7	0.58	0.2950	0.0271	0.0400	0.0010	0.2647	252.9	6.0	96%
	LJ13-22	234.1	263.8	0.89	0.2797	0.0220	0.0397	0.0010	0.3119	251.0	6.0	99%
	LJ13-23	167.4	500.5	0.33	0.2873	0.0171	0.0398	0.0007	0.2815	251.7	4.1	98%

	LJ13-24	69.3	116.2	0.60	0.2811	0.0239	0.0398	0.0010	0.2969	251.6	6.2	99%
	LJ13-25	376.8	715.2	0.53	0.2844	0.0140	0.0400	0.0007	0.3381	253.0	4.1	99%
	LJ13-10	228.3	285.8	0.80	11.0508	0.3111	0.4767	0.0060	0.4437	2513.1	26.0	99%
	LJ13-20	56.4	100.4	0.56	10.8981	0.3830	0.4763	0.0082	0.4898	2511.1	35.8	99%

Table 2. Results of analyses of $\delta^{13}C_{org}$, TOC, trace and major elements, Ni/Al, Th/U, CIA_{corr} and kerogen macerals

Sample number	$\delta^{13}C_{org}$ (‰)	TOC (%)	Trace elements (ppm)			Major elements (%)					Ni/Al	Th/U	CIA_{corr}	Kerogen maceral (%)			
			Th	U	Ni	Al_2O_3	CaO	Na_2O	Ka_2O	P_2O_5				Saprop elinite	Exinite	Vitrinite	Intertinite
LJ6	-27.3	0.11	10.40	2.46	9.44	19.73	1.89	0.51	5.01	0.41	0.48	4.23	82.04	14.1	12.2	18.0	55.7
LJ11	-27.6	0.08	10.40	2.17	10.20	16.58	2.83	0.70	3.67	0.27	0.62	4.79	78.14	19.3	2.3	21.6	56.8
LJ12	-27.2	0.11	10.00	2.30	11.20	14.13	1.72	0.48	3.67	0.15	1.50	4.35	80.05	14.3	2.4	18.5	64.8
LJ13	-27.0	0.13	11.90	3.79	34.78	15.28	0.61	0.77	3.67	0.04	2.28	3.14	77.39	9.3	2.5	15.4	72.8
LJ16	-27.6	0.08	15.70	3.93	23.30	14.13	0.58	1.39	3.27	0.03	1.65	3.99	73.25	19.4	7.5	16.0	57.1
LJ17	-26.8	0.04	20.30	4.65	25.30	19.68	1.08	1.17	5.11	0.05	1.29	4.37	74.65	3.8	7.6	7.6	81.0
LJ18	-27.0	0.12	12.90	3.6	15.80	14.16	1.24	1.65	2.99	0.03	1.12	3.54	72.74	17.7	1.6	8.0	72.7

LJ18-1	-28.6	0.10	13.10	4 3.70	17.20	14.08	1.27	1.61	3.05	0.05	1.22	3.54	71.03	13.5	1.1	7.2	78.3
LJ19	-27.9	0.09	13.30	3.87	18.40	14.00	1.29	1.15	3.11	0.07	1.31	3.44	70.06	9.2	0.6	6.3	83.9
LJ27	-24.9	16.00	13.20	3.88	10.80	16.30	0.63	0.75	3.60	0.05	0.66	3.40	78.15	21.5	9.5	8.0	61.0
LJ30	-24.0	0.17	13.20	3.86	10.60	17.30	0.73	0.73	4.09	0.03	0.61	3.42	78.15	24.1	10.3	9.8	55.7
LJ32	-23.1	0.13	17.50	6.61	3.67	21.32	0.74	1.21	4.13	0.08	0.17	2.65	77.54	90.0	1.0	8.0	1.0
LJ34	-24.3	0.19	24.40	7.93	20.60	20.13	0.61	1.25	4.53	0.04	1.02	3.08	77.55	34.9	9.6	50.6	4.8
LJ39	-23.3	0.08	23.40	5.99	20.70	20.10	0.41	1.85	4.47	0.03	1.03	3.91	75.12	10.9	16.8	63.4	8.9
LJ40	-23.8	0.14	18.70	6.26	22.90	19.43	1.20	1.72	3.94	0.04	1.18	2.99	73.53	40.4	1.3	50.6	7.7
LJ44	-26.5	0.11	16.90	4.98	20.80	18.00	1.14	1.32	3.96	0.10	1.16	3.39	72.75	16.6	3.8	61.6	18.0
LJ46	-25.3	0.15	14.70	4.31	15.10	17.59	1.60	1.38	3.58	0.16	0.86	3.41	70.74	38.9	27.8	16.7	16.7
LJ50	-26.1	0.15	13.70	3.56	23.50	16.67	1.80	1.35	3.54	0.02	1.41	3.85	70.27	19.6	12.5	48.2	19.6
LJ51	-26.3	0.18	12.50	3.38	22.50	14.47	1.88	1.28	3.06	0.03	1.55	3.70	68.94	31.6	0.0	57.9	10.5
LJ52	-27.1	0.13	12.50	3.90	24.60	23.03	1.47	2.62	5.15	0.03	1.07	3.21	68.42	19.6	12.5	48.2	19.6
LJ53	-25.5	0.11	12.30	4.41	23.60	17.15	1.44	1.62	3.62	0.13	1.38	2.79	68.97	31.6	0.0	57.9	10.5
LJ5	-26	0.1	15.	4.	21.	14.	1.	0.7	3.1	0.	1.4	3.	76.	4.9	4.6	84.0	6.6

9	.8	2	20	22	80	81	36	5	7	02	7	60	32				
LJ60	-28.1	0.17	19.50	4.75	18.00	16.30	1.09	0.67	3.53	0.04	1.10	4.11	78.47	5.0	6.0	38.2	50.7
LJ61	-27.5	0.10	25.00	7.30	9.52	18.26	1.16	0.71	4.05	0.07	0.52	3.42	78.94	28.0	8.0	36.0	28.0
LJ72	-26.0	0.13	15.60	3.60	20.60	17.82	1.79	0.77	4.31	0.11	1.16	4.33	77.97	7.2	9.5	57.2	26.1
LJ73	-26.8	0.09	19.70	4.78	13.60	20.34	1.21	0.89	4.87	0.03	0.67	4.12	77.79	1.5	1.5	69.2	27.7
LJ75	-26.4	0.08	17.30	4.16	11.10	16.39	1.25	0.82	3.97	0.02	0.68	4.16	76.47	19.5	6.1	52.4	22.0
LJ76	-26.0	0.10	20.10	4.81	12.00	22.47	2.98	1.02	5.16	0.0[illegible]	0.53	4.18	77.43	10.4	2.6	63.6	23.4

Declaration of interests

☒ The authors declare that they have no known competing financial interests or personal relationships that could have appeared to influence the work reported in this paper.

☐The authors declare the following financial interests/personal relationships which may be considered as potential competing interests:

Diachronous end-Permian terrestrial ecosystem collapse with its origin in wildfires

Jing Lu, Ye Wang, Minfang Yang, Peixin Zhang, David P. G. Bond, Longyi Shao, Jason Hilton

Highlights

- The PT boundary is radioisotopically constrained on the North China Plate
- Catastrophic soil erosion marks the onset of terrestrial losses prior to the PTB
- Extinctions in North China began in terrestrial settings before the marine crisis
- Humid/arid conditions promoted frequent wildfires that were responsible for losses
- End Permian Terrestrial Collapse led to marine crisis through a cascade of effects

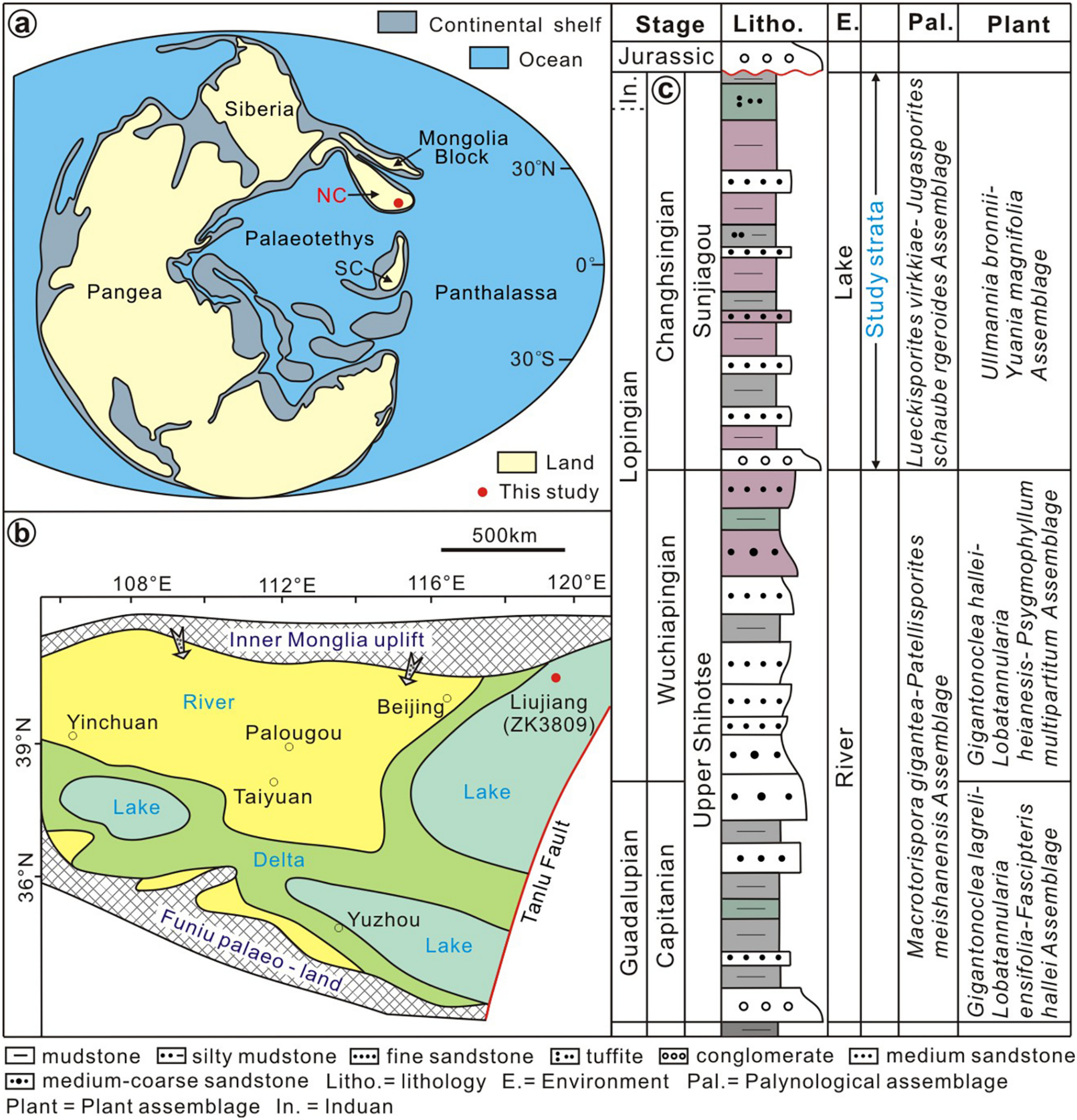

a
Continental shelf
Ocean
Siberia
Mongolia Block
30°N
NC
Palaeotethys
0°
SC
Pangea
Panthalassa
30°S
Land
This study
b
500km
108°E
112°E
116°E
120°E
Inner Monglia uplift
River
Beijing
Liujiang (ZK3809)
Yinchuan
Palougou
39°N
Taiyuan
Lake
Lake
Delta
36°N
Yuzhou
Lake
Tanlu Fault
Funiu palaeo - land
Stage
Litho.
E.
Pal.
Plant
Jurassic
In.
c
Lopingian
Changhsingian
Sunjiagou
Lake
Study strata
Lueckisporites virkkiae- Jugasporites schaube rgeroides Assemblage
Ullmannia bronnii- Yuania magnifolia Assemblage
Wuchiapingian
Upper Shihotse
River
Macrotorispora gigantea-Patellisporites meishanensis Assemblage
Gigantonoclea hallei- Lobatannularia heianesis- Psygmophyllum multipartitum Assemblage
Guadalupian
Capitanian
Gigantonoclea lagreli- Lobatannularia ensifolia-Fascipteris hallei Assemblage
mudstone
silty mudstone
fine sandstone
tuffite
conglomerate
medium sandstone
medium-coarse sandstone
Litho.= lithology
E.= Environment
Pal.= Palynological assemblage
Plant = Plant assemblage
In. = Induan

Figure 1

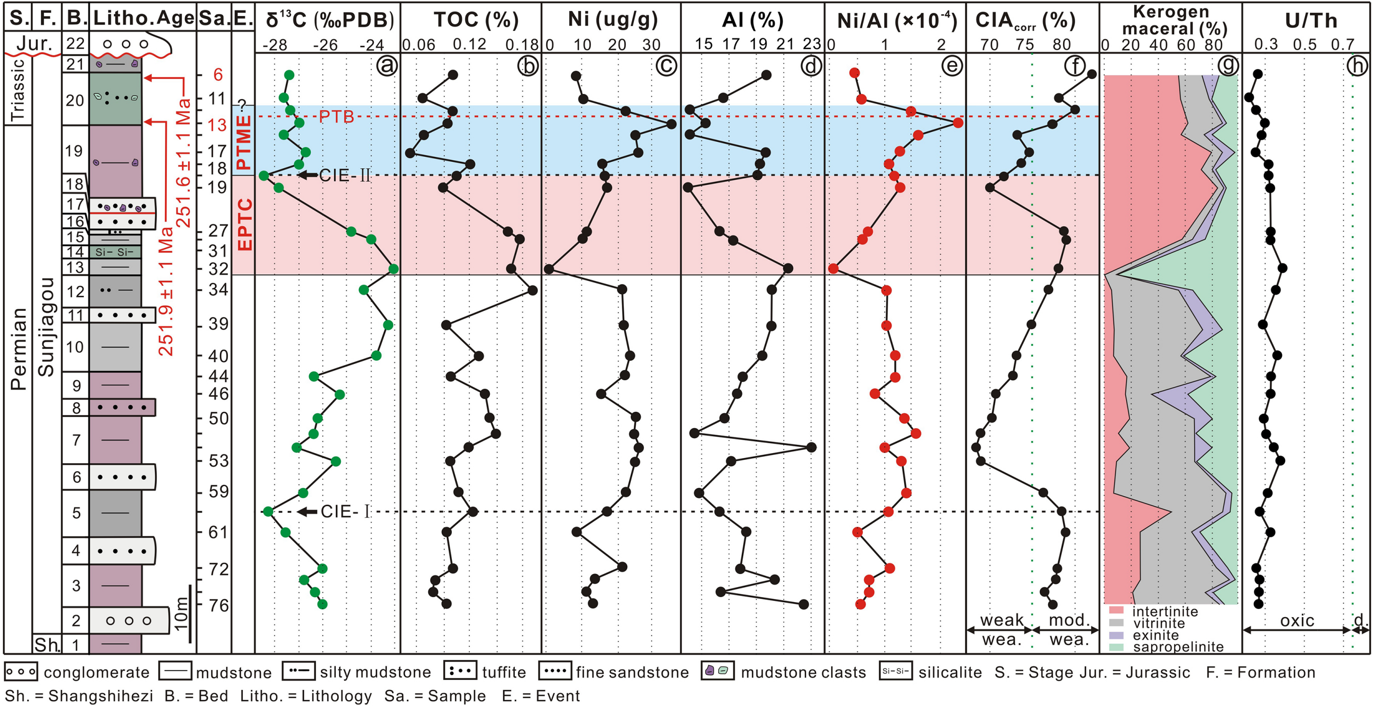

S.
F.
B.
Litho.
Age
Sa.
E.
δ13C (‰PDB)
TOC (%)
Ni (ug/g)
Al (%)
Ni/Al (×10-4)
CIAcorr (%)
Kerogen maceral (%)
U/Th
Jur.
Triassic
Permian
Sunjiagou
Sh.
PTME
EPTC
PTB
CIE-II
CIE-I
251.6 ±1.1 Ma
251.9 ±1.1 Ma
10m
weak wea.
mod. wea.
oxic
d.
intertinite
vitrinite
exinite
sapropelinite
conglomerate
mudstone
silty mudstone
tuffite
fine sandstone
mudstone clasts
silicalite
S. = Stage Jur. = Jurassic F. = Formation
Sh. = Shangshihezi B. = Bed Litho. = Lithology Sa. = Sample E. = Event

Figure 2

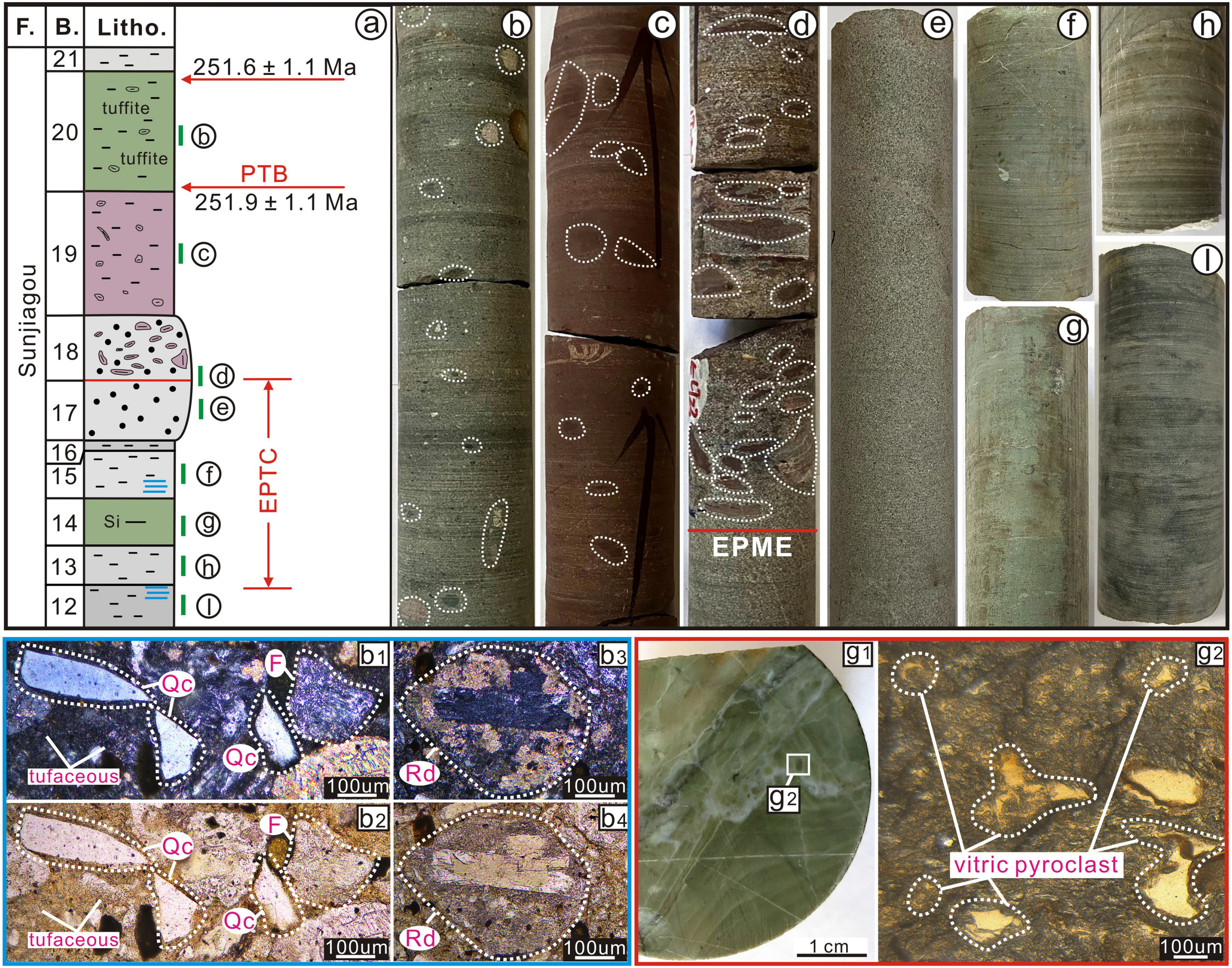
F.
B.
Litho.
a
Sunjiagou
21
20
19
18
17
16
15
14
13
12
tuffite
tuffite
Si
251.6 ± 1.1 Ma
PTB
251.9 ± 1.1 Ma
EPTC
b
c
d
e
f
g
h
l
EPME
b1
b2
b3
b4
Qc
F
tufaceous
Rd
100um
g1
g2
1 cm
vitric pyroclast

Figure 3

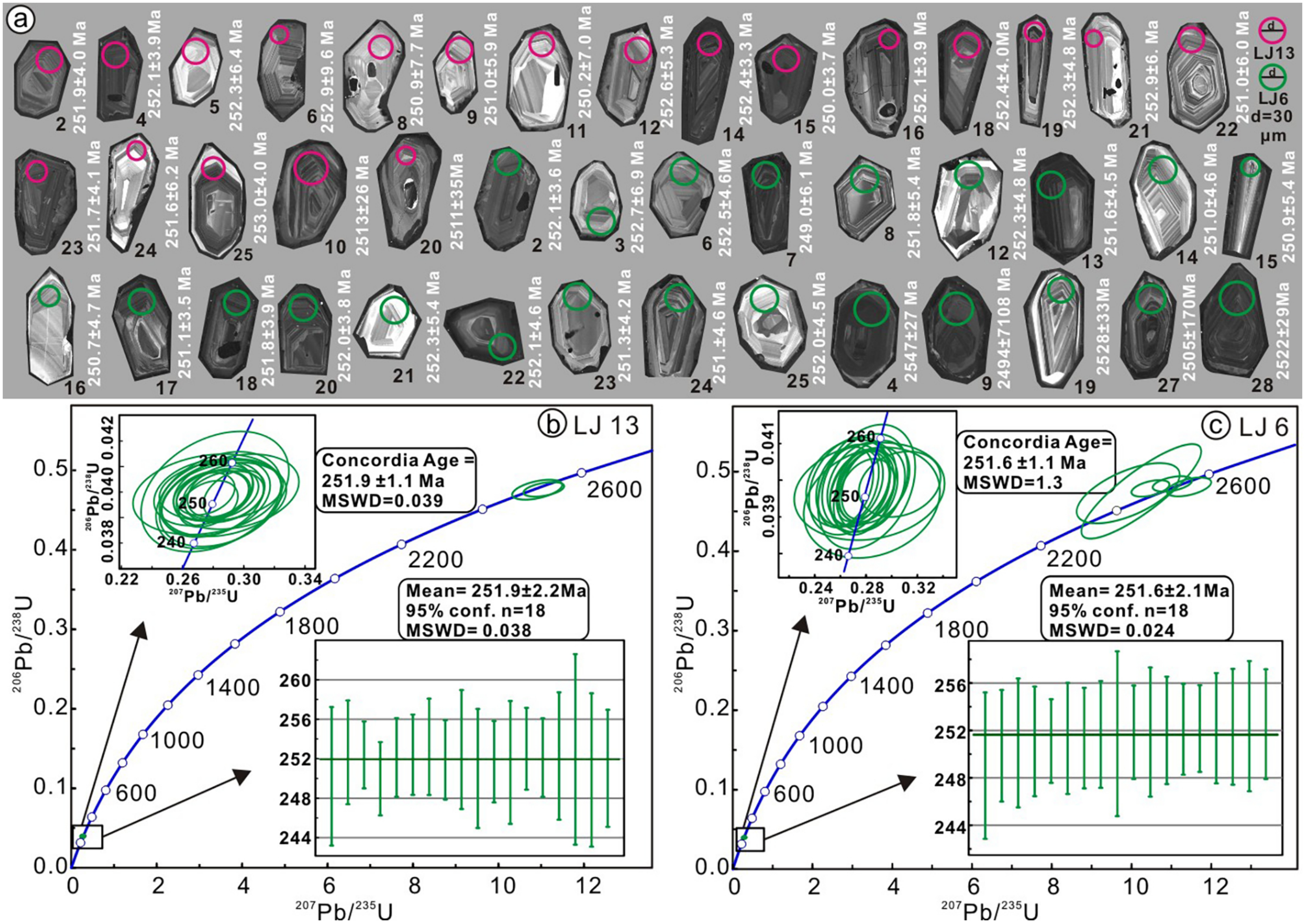
a
b LJ 13
Concordia Age = 251.9 ±1.1 Ma MSWD=0.039
Mean= 251.9±2.2Ma 95% conf. n=18 MSWD= 0.038
c LJ 6
Concordia Age= 251.6 ±1.1 Ma MSWD=1.3
Mean= 251.6±2.1Ma 95% conf. n=18 MSWD= 0.024
LJ13
LJ6
d=30 μm

Figure 4

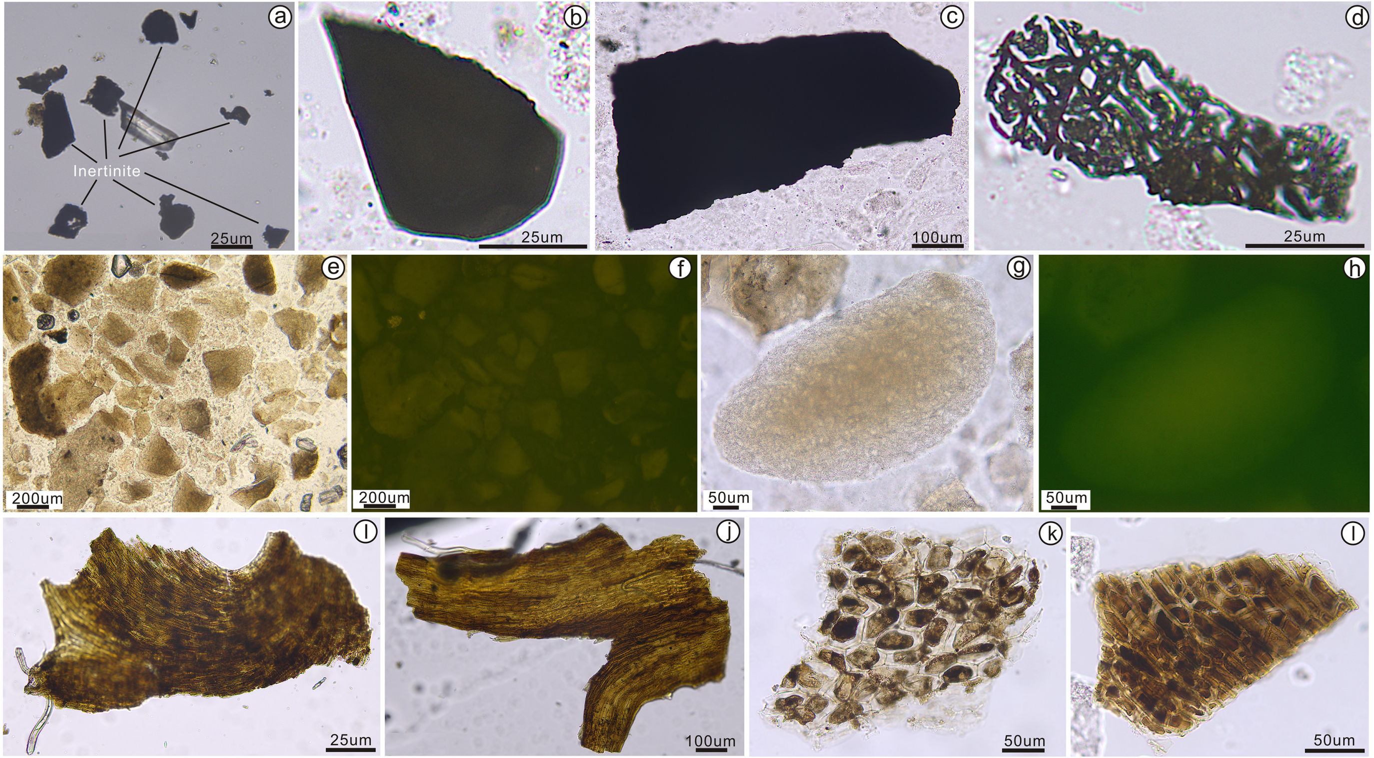
a
Inertinite
25um
b
25um
c
100um
d
25um
e
200um
f
200um
g
50um
h
50um
I
25um
j
100um
k
50um
l
50um

Figure 5

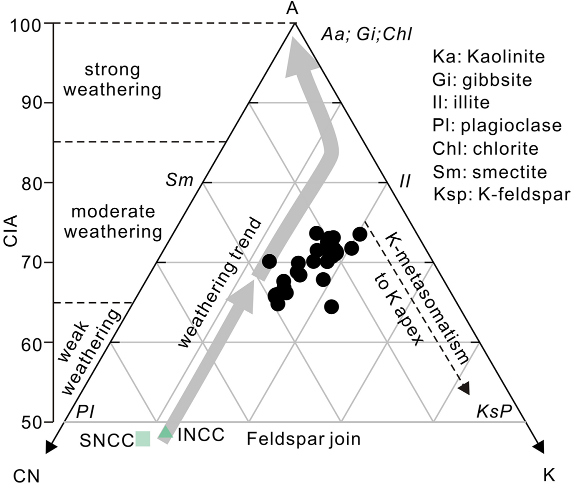

A
Aa; Gi;Chl
Ka: Kaolinite
Gi: gibbsite
Il: illite
Pl: plagioclase
Chl: chlorite
Sm: smectite
Ksp: K-feldspar
100
90
80
70
60
50
CIA
strong weathering
moderate weathering
weak weathering
Sm
Il
Pl
KsP
weathering trend
K-metasomatism to K apex
SNCC
INCC
Feldspar join
CN
K

Figure 6

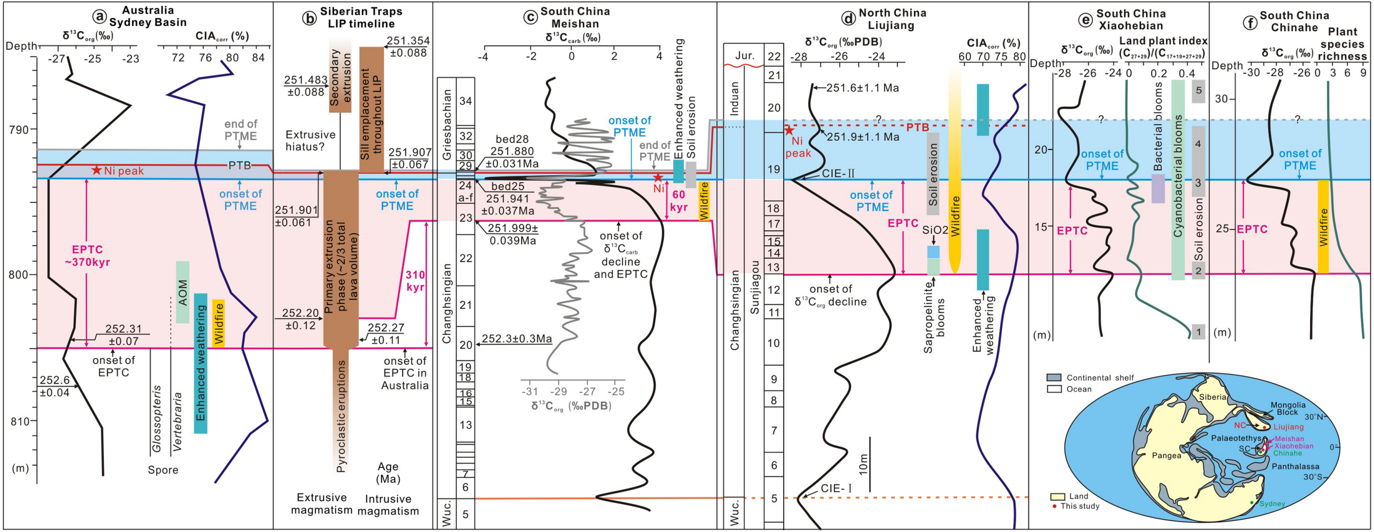

a Australia Sydney Basin
b Siberian Traps LIP timeline
c South China Meishan
d North China Liujiang
e South China Xiaohebian
f South China Chinahe
PTB
Ni peak
onset of PTME
end of PTME
EPTC ~370kyr
onset of EPTC
Wildfire
Enhanced weathering
Soil erosion
AOM
Glossopteris
Vertebraria
Spore
Primary extrusion phase (~2/3 total lava volume)
Sill emplacement throughout LIP
Secondary extrusion
Pyroclastic eruptions
Extrusive magmatism
Intrusive magmatism
Age (Ma)
310 kyr
60 kyr
CIE-I
CIE-II
Sapropelinite blooms
Bacterial blooms
Cyanobacterial blooms
Land plant index
Plant species richness
Continental shelf
Ocean
Land
This study
Pangea
Siberia
Panthalassa
Palaeotethys
Liujiang
Meishan
Xiaohebian
Chinahe
Sydney

Figure 7